# Postfire residual capacity of steel fiber reinforced volcanic scoria concrete using

# PSO-BPNN machine learning

Bin Cai[a], Xiaqi Lin[a], Feng Fu[b*], Lin Wang[a].

[a] School of Civil Engineering, Jilin Jianzhu University, Changchun 130118, Jilin, China
[b] School of Mathematics, Computer Science and Engineering, City, University of London, London, UK:

**Abstract**

Volcanic scoria (VS) is a potential green aggregate, as it is abundant around the world. Replacing normal aggregate with VS aggregate improves economic efficiency, ecological benefits in the construction industry. In this study, an artificial neural network (ANN) is employed to predict the behavior of steel fiber reinforced volcanic scoria concrete (SFVSC). Compression strength (CS) and tensile splitting strength (STS) tests on SFVSC was first conducted to obtain 240 groups of training data. Based on the training data, appropriate neural network structures and training processes was established using several neural network models. The behavior of steel fiber volcanic scoria concrete is predicted with various parameters. The prediction accuracy of is appraised using the mean absolute percentage error (MAPE), root mean square error (RMSE), and correlation coefficient ($R^2$) for different machine learning algorithm back propagation neural network (BPNN), genetic algorithm (GA-BPNN), and particle swarm optimization (PSO-BPNN). The main conclusion is that the PSO-BPNN model outperforms the other models in prediction accuracy. The other results show that both GA-BPNN and PSO-BPNN exhibit good accuracy and suitable in predicting the mechanical properties of SFVSC. Using machine learning, the effect of different VS aggregate replacement levels (VR) (30, 50, 70%), steel fiber dosage ($V_{st}$) (0, 0.5, 1, 1.5%), water-to-cement ratios (w/b) (0.4, 0.5), and temperatures (t) (20, 200, 400, 600, 800°C) on the mechanical properties of SFVSC is also studied.

**Keywords:** Volcanic scoria; Steel fiber; Fire; Compressive strength; Split tensile strength; PSO-BP neural network.

---

## 1. Introduction

Architectural design is increasingly evolving towards wide spans, huge bearings, and high-rise numbers in many current architectural applications. Plain concrete is a basic building material, compounded with cement, water, aggregates, and mineral or chemical additives. Plain concrete makes the structure of a building more stable because of its inherent higher self-weight, but it is also more susceptible to earthquake effects. Moreover, the solution of increasing the size of vertical members in order to meet the building requirements of high-rise buildings can also cause certain obstacles to the architectural design. Light aggregate concrete is a special type of concrete, which aggregate is lighter than plain concrete. Light aggregate concrete has the advantages of excellent thermal insulation, fire resistance, seismic resistance, and permeability resistance [1]. Transportation, reinforcing, and foundation costs are all reduced when using light aggregate concrete. Volcanic scoria is a high-quality natural light aggregate with low thermal conductivity and high porosity [2]. It has a light mass, is frost and crack resistant, and has low thermal conductivity. The application of volcanic scoria, as a green building material, also reduces the environmental damage caused by natural stone [3-8]. Because volcanic scoria has a high porosity, it reduces the risk of explosive concrete shedding produced by pore pressure build-up generated by internal steam when the concrete is heated [9]. Volcanic scoria concrete provides excellent thermal insulation capabilities. Volcanic scoria concrete's exceptional fire resistance can be employed in a wide range of construction applications. Everyday settings that expose

the concrete to high temperatures include fires, machinery that emits high temperatures, and fireplaces, to name a few. High temperature is one of the most important physical effects on the durability of concrete [2]. Concrete's mechanical properties, such as modulus of elasticity, compressive strength, and splitting tensile strength, are considerably reduced when subjected to high temperatures. The load-bearing capacity of concrete after exposure to high temperatures is crucial to investigating and determining the mechanical properties of concrete after exposure to high temperatures usually needs a large number of trials.

As experiments are costly and time-consuming, it is not always possible to do experiments to obtain the mechanical properties of concrete. To obtain these mechanical properties of concrete, researchers have used several methods such as regression methods, statistical methods, artificial neural networks, and so forth [10]. Among these, artificial neural networks have attracted much attention. Numerous studies have shown that artificial neural networks can be used in civil engineering with outstanding results, such as concrete carbonation depth prediction, mechanical property prediction of recycled aggregate concrete, soil compression coefficient prediction, concrete crack width prediction, and so on [11-17]. Artificial neural networks have gained wide attention and application mainly because they have the advantages of self-organization, self-learning, and self-adaptability, and can perform classification, prediction, and pattern recognition, which can effectively solve various complex engineering problems [10, 18].

Common artificial neural networks such as BP neural networks have the advantage

of robustness, but the models converge slowly and tend to fall into local minima [19, 20]. To address these drawbacks, many studies have applied intelligent global optimization algorithms such as genetic algorithm and particle swarm algorithm to optimize neural networks [21-24]. A. Ismail et al. applied the PSO-BP model to predict the load-deformation properties of axial compression piles [25]. These studies demonstrated that optimization algorithms such as particle swarm algorithm and genetic algorithm are very effective in improving neural networks, increasing the predictive effectiveness and computational efficiency of the relevant models [13]. In particular, it is noted in the paper that particle swarm algorithm usually converges faster than genetic algorithm in the computational process [26]. To the extent of our knowledge, optimization of back-propagation neural networks using particle swarm optimization algorithm has not been attempted in the prediction of postfire residual strength of concrete.

The main purpose of this study was to develop a neural network model to predict the compressive and split tensile strength of SFVSC after fire at 28 days. In this paper, the compressive strength and split tensile strength of SFVSC after fire were obtained from experiments, and a test database was established. Three models (BPNN, GA-BPNN, PSO-BPNN) were applied to predict the residual strength of concrete with volcanic scoria replacement level, temperature, the volumetric fraction of steel fiber, and water-to-cement ratio as input variables. In the end, the superiority of the models was evaluated by analyzing the prediction results.

## 2. Experimental database

### 2.1 Materials

Figure 1 and Table 1 show the raw materials used in this experiment and their specific information. The raw materials for this test include volcanic scoria, ordinary river sand, ordinary gravel, P.042.5 ordinary silicate cement, and steel fiber. The volcanic scoria selected for this test was from Guzhanzi, Huinan County, Changchun City, Jilin Province, China.

**Table 1**
**Fig.1**

Table 2 and Figure 2 summarize the chemical composition and aggregate grading of the materials used in the concrete and their physical properties. All processed experimental results were used in the prediction process of the neural network.

**Table 2**
**Fig.2**

### 2.2 Mixtures

In this test, a total of 24 proportions were designed based on three volcanic scoria replacement levels (30, 50, 70%), two water-to-cement ratios (0.4, 0.5), and four volumetric fractions of steel fiber (0, 0.5, 1, 1.5%), and a total of 720 SFVSC test blocks were configured. The details of the proportions are shown in Table 3.

**Table 3**

### 2.3 Test block preparation、experiment and testing methods

Block production and testing process: 1) The (JG151-2002) (CABR2003) Technical Specification for Lightweight Aggregate Concrete [27]was used to design and produce 720 standard cubic test blocks with a grade LC30 design strength and an

average density of 1976.23 kg/m$^3$. A total of 360 test blocks were subjected to a compressive strength (CS) test, and the remaining blocks were subjected to a split tensile strength (STS) test. Groups of three blocks were tested under the same conditions, and the average of the three test results for each group was used for neural network prediction. A total of 240 groups of data were obtained, including 120 groups of CS test data and 120 groups of STS test data. 2) Test blocks were constructed and subjected to a fire test. 3) CS and STS tests were performed on the fire-treated test blocks. The testing method complied with the Standard of Testing Methods for Mechanical Properties of Ordinary Concrete (GB/T 50081-22002) [28]. Fig. 3 shows the fabrication and test processes for the blocks.

**Fig.3**

## 2.4 Experimental database

A total of 240 groups of data were obtained from the tests, including 120 sets of compressive strength test data and 120 sets of split tensile strength test data. An experimental database was established with these data.

## 2.5 Correlation between compressive strength and split tensile strength.

Fig. 4 presents the relationship between the CS and STS obtained by processing the experimental data and Formula (1) is the corresponding regression formula. The regression coefficient ($R^2$) is 0.983755. An $R^2 \geq 0.85$[29] shows that the fitting parameters are correlated. The CS and the STS are correlated.

$$f_{t \cdot s} = 0.0212 f_c^{1.376} \tag{1}$$

**Fig.4**

## 3. Artificial neural network

### 3.1 Introduction to the back propagation neural network

Back propagation neural networks (BPNNs) are currently widely applied. There are two learning stages in BPNNs forward propagation of signals and back propagation of errors. A signal processed by the network during forward propagation that does not reach the termination requirement is transferred to the back propagation stage as an error signal. Each neuron dynamically adjusts its own weights and thresholds according to the error signal to the end of this round. The weight is corrected from round to round. When the error of the output signal meets the accuracy requirement, the network is established. The BPNN model transforms a problem into a mathematical optimization problem. The network can approximate any nonlinear mapping given a sufficient number of hidden layers of neuron points. As the initial weights and thresholds of the network are randomly selected, the network is prone to fall into local minima.

### 3.2 Introduction to genetic algorithm optimized back propagation neural network

The genetic algorithm (GA) is a simulated evolutionary algorithm that is applicable to any class of functions with or without specified functional forms. The GA can be used for parallel computing and offers the following advantages: high robustness, strong global searchability, and facile calculations. GA can evolve populations continuously through processes such as selection, crossover, and mutation, to obtain optimal solutions. In this study, the GA is used to refine the weights and thresholds of a neural network to improve the prediction speed and accuracy. Fig. 5 is a flow diagram

for the GA used to optimize the BP neural network:

Step 1 Establish BP neural network, determine the network structure, transfer function, and learning rules.

Step 2 Collect raw data such as temperature, the volumetric fraction of steel fiber, volcanic scoria replacement level, and water-to-cement ratio, and normalize the raw data for pre-processing, and the pre-processed values are used as the input values of the network.

Step 3 Select the parameters of the genetic algorithm and initialize the population.

Step 4 Determine the individual's fitness in the population $F(i)$. The expression function is shown in Equation (2):

$$F(i)=\sum_{i=1}^{n} abs\left(y_i - y_i^{'}\right) \tag{2}$$

where n is the number of network output nodes, $y_i$ is the desired output, and $y_i^{'}$ is the predicted output value.

Step 5 Genetic evolution of populations. Perform the operations of selection, crossover, and mutation in genetic algorithm to retain individuals with high fitness and eliminate those with low fitness.

Step 6 Calculate the individual fitness value again, and if there are individuals in the new population that make the network reach global convergence, or if the number of iterations reaches the set maximum, record the individual with the highest fitness and proceed to the next step, otherwise return to Step 5.

Step 7 Output the individual with the highest fitness value to obtain the weights and thresholds that make the global optimum.

Step 8 The optimal initial weights and thresholds obtained by the genetic algorithm are given to the BP neural network, and then the BP neural network is trained using the reserved training samples until the error reaches the target interval, completing the construction of the model.

Step 9 The pre-processed data are fed into the trained GA-BP neural network, and the network output data are inverse normalized to obtain the predicted postfire residual strength of SFVSC.

**Fig.5**

### 3.3 Introduction to particle swarm optimization optimized back propagation neural network

The particle swarm optimization (PSO) algorithm is an evolutionary computation technology based on swarm intelligence. PSO is similar to GA but does not perform crossover and mutation operations. Instead, PSO searches for the optimal solution by using changes in the particle position to locate the optimal particle position in the solution space. PSO is an efficient optimization algorithm with a simple principle and mechanism that does not require gradient information and has few adjustable parameters. Thus, the algorithm is easy to implement and run efficiently. Considering the disadvantages of the BPNN exist, PSO is used in this study to optimize the weights and thresholds of the BP neural network. Fig.6 is a flow diagram of the PSO used to optimize the BP neural network:

Step 1 Establish BP neural network, determine the network structure, transfer function, and learning rules.

Step 2 Collect raw data such as temperature, the volumetric fraction of steel fiber,

volcanic scoria replacement level, and water-cement ratio, and normalize the raw data for pre-processing, and the pre-processed values are used as the input values of the network.

Step 3 Select the parameters of the PSO algorithm and initialize the population.

Step 4 Determine the fitness function *Fitness* as in Equation (3), which is used to guide the search behavior of the population and calculate the fitness value of the particles.

$$Fitness = \frac{1}{M}\sum_{i=1}^{M}\sum_{j=1}^{N}\left(a_{ij} - b_{ij}\right)^2 \qquad (3)$$

where $M$ is the total number of study samples, $N$ is the number of output nodes, $a_{ij}$ is the actual output value of the corresponding parameter, $b_i$ is the desired output value of the corresponding parameter.

Step 5 Compare the current and pre-iteration fitness of individual particles. If the current fitness of the particle is better than the pre-iteration fitness, the update of the particle's best position $p_b$ is performed. For the swarm best position $p_{gb}$, among all the particle best positions, the particle best position with the best fitness is the swarm best position. The swarm's best position corresponds to the weight and thresholds of the neural network for the current optimal solution of the particle population.

Step 6 The velocity and position of the particle are updated using equations (4) and (5).

$$v_{i+1}\left(t+1\right) = \omega v_i\left(t\right) + c_1 r_1 \left(p_{bi}\left(t\right) - x_i\left(t\right)\right) + c_2 r_2 \left(p_{gb} - x_i\left(t\right)\right) \qquad (4)$$

$$x_{i+1}\left(t+1\right) = x_i\left(t\right) + v_{i+1}\left(t+1\right) \qquad (5)$$

where $v_i$ is the velocity vector, $x_i$ is the position vector, $\omega$ is inertial weight, $c_1$ and $c_2$

are learning factors, $r_1$ and $r_2$ are two random values between 0 and 1.

Step 7 Determine if the termination condition is reached. If the current number of iterations reaches the maximum number set or the error meets the minimum error set, the algorithm stops iterating and moves to the next step, otherwise, it goes to Step 4.

Step 8 Output the $p_b$ corresponding to the current fitness value as the global optimal solution, at this time the obtained weights and thresholds are the optimal initial weights.

Step 9 Substitute the PSO-optimized weights and thresholds into the BP neural network, train the PSO-optimized neural network with training samples until the error is met, and complete the construction of the model.

Step 10 The pre-processed data are fed into the trained PSO-BP neural network and the network output is inversely normalized to derive the predicted postfire residual strength of SFVSC.

**Fig.6**

## 4. Artificial neural network prediction model

### 4.1 Model development

In this study, BPNN1, GA-BPNN1, and PSO-BPNN1 models are established to predict the CS of concrete, and BPNN2, GA-BPNN2, and PSO-BPNN2 models are established to predict the STS of concrete. The following network structures used are presented below.

(i) Four input-layer neurons are used: temperature (20, 200, 400, 600, 800°C), volumetric fraction of steel fiber (0, 0.5, 1, 1.5%), volcanic scoria replacement level

(30, 50, 70%), and water-to-cement ratio (0.4, 0.5).

(ii) The output-layer neurons are the CS and STS of the SFVSC.

(iii) All four ANN models are three-layer network structures with only one hidden layer.

An effective appropriate theory that can determine the number of required hidden layer neurons (HLNs) for a specific problem has not yet been developed. Formula (6) is used to set the number of neurons 4-13. The optimal number of HLNs is determined by the root mean square error (RMSE). The results are shown in Table 4.

$$n_h = \sqrt{n_{in} + n_o} + \mathrm{m} \tag{6}$$

where $n_h$ is the number of hidden nodes, $n_{in}$ is the number of input layer nodes, $n_o$ is the number of output layer nodes, and m is a regulation constant ranging from 1 to 10.

**Table 4**

The following neural network settings were used in this study.

(i) A total of 7 hidden nodes were used in BPNN1, GA-BPNN1, and PSO-BPNN1, with a training target error of 0.0001, a maximum number of training steps of 1000, and a learning rate of 0.1.

(ii) A total of 6 hidden nodes were used in BPNN2, GA-BPNN2, and PSO-BPNN2, with a training target error of 0.0001, a maximum number of training steps of 1000, and a learning rate of 0.1.

The activation function for the HLNs was the tangent sigmoid function, and the output is controlled at [0,1], which is the optimal setting for the current application [30], see Formula (7).

$$f(x) = \frac{1}{1+e^{-x}} \tag{7}$$

Data often need to be preprocessed before being input into a network. Data normalization is a common data preprocessing method that transforms input and output data to lie within the [0,1] interval, as shown in Formula (8):

$$X_{i,t} = \frac{X_i - X_{min}}{X_{max} - X_{min}} \tag{8}$$

where $X_i$ is an input/output datum, and $X_{min}$ and $X_{max}$ are the minimum and maximum values in the data range, respectively.

Fig. 7 shows the topological structure of the neural network.

Fig.7

## 4.2 Input and output parameters of neural networks

The experimental database yields 120 groups of CS data and 120 groups of STS data. A total of 90 groups of CS data are utilized for network training, and the remaining 30 groups of data are used for network testing. The STS groups are likewise divided into training and testing groups. The variables used for training and testing include $t$(20, 200, 400, 600, 800°C), $V_{st}$(0, 0.5, 1, 1.5%), VR(30, 50, 70%), and w/b(0.4, 0.5).

## 4.3 Predictions and discussion

To determine the efficacy of GA-BPNN and PSO-BPNN, the predictions of these models are compared against those of BPNN. The performance of the prediction models is evaluated using the MAPE and the RMSE. The model robustness is assessed by the correlation coefficient ($R^2$).

$$\text{MAPE} = \frac{1}{n}\sum_{i=1}^{n}\frac{|a_i - b_i| \times 100\%}{a_i} \tag{9}$$

$$\text{RMSE} = \sqrt{\frac{1}{n}\sum_{i=1}^{n}(a_i - b_i)^2} \tag{10}$$

$$R^2 = 1 - \left( \frac{\sum\limits_{i=1}^{N} (a_i - b_i)^2}{\sum\limits_{i=1}^{N} b_i^2} \right) \tag{11}$$

In the equation above, $a_i$ is the test strength of the concrete, $b_i$ is the neural network prediction, and $n$ is the total number of blocks used for neural-network training and testing.

Fig. 8 shows that the result does not change at 46, 48, 60, and 64 and reaches the maximum value.

**Fig.8**

PSO-BPNN, GA-BPNN, and BPNN are used to predict the residual bearing capacity of SFVSC subjected to high-temperature treatment, and the results are compared against the actual in Fig. 9. There is little difference between the prediction of the trained PSO-BPNN, GA-BPNN, and BPNN models and the actual values. However, PSO-BPNN makes the prediction closest to the target value and is, therefore, the most accurate model.

**Fig.9**

Fig. 10 shows that PSO-BPNN yields the most accurate prediction, where the absolute error in the PSO-BPNN prediction is enclosed by that of the GA-BPNN prediction. Furthermore, the absolute error produced by the GA-BPNN prediction is enclosed by that of the BPNN prediction. Thus, the prediction accuracy in terms of the absolute error decreases in the following order: PSO-BPNN > GA-BPNN > BPNN.

**Fig.10**

Fig. 11 shows that PSO-BPNN yields the most accurate prediction result. The relative error in the PSO-BPNN prediction is smaller than that in the GA-BPNN prediction, which in turn is smaller than that in the BPNN prediction. Thus, the

prediction accuracy in terms of the MAPE decreases in the following order: PSO-BPNN > GA-BPNN > BPNN.

**Fig.11**

Table 5 shows the performances of the various neural network models. The prediction accuracy decreases in the following order: PSO-BPNN > GA-BPNN > BPNN. Both the performance evaluation parameters for the PSO-BPNN1 CS prediction are better than those of the GA-BPNN1 and BPNN1 prediction (1.01%(MAPE) and 0.3332(RMSE)). Both the performance evaluation parameters for the PSO-BPNN2 STS prediction are better than those of the GA-BPNN2 and BPNN2 STS prediction (1.62%(MAPE) and 0.0488(RMSE)).

**Table 5**

Figs. 12-and 13 show the robustness of BPNN, GA-BPNN, and PSO-BPNN for 90 groups of training samples and 30 groups of test samples. Table 6 shows the $R^2$ for each model for training and testing. The $R^2$ of PSO-BPNN is closer to 1 than that of GA-BPNN, which in turn is closer to 1 than that of BPNN. The robustness of the models shows that the generalization ability of the models decreases in the following order: PSO-BPNN > GA-BPNN > BPNN.

**Table 6**
**Fig.12**
**Fig.13**

## 5. Parametric study of concrete strength using machine learning

Since the prediction result is satisfactory, this paper used the PSO-BPNN to evaluate the effect of different parameters on the strength of SFVSC. Different key parameter values were input into the machine for strength prediction. Based on the

prediction result, we further studied how different parameters affect the strength of SFVSC. The results are shown below.

## 5.1 Effect of volcanic scoria replacement level

The effect of VR on strength is investigated. The input values were as follows: $t =$ 20, 200, 400, 600, and 800°C; $V_{st} = 1\%$; VR = 0, 10, 20, 30, 40, 50, 60, 70, 80, 90, and 100%; and w/b = 0.4. Fig. 14 shows the response of SFVSC strength with VR. It can be seen from the figure that an increase in VR leads to a decrease in the SFVSC strength. Since VS aggregate has a low strength of its own, it is the scoria and cement stone itself rather than the bonded interface between the aggregate and cement stone that is first damaged by the force when the concrete is damaged. As the concrete in the VR increases and the gravel content decreases, the overall strength of the aggregate decreases, eventually causing a significant reduction in concrete strength.

**Fig.14**

## 5.2 Effect of temperature

The effect of $t$ on strength is studied. The input values were as follows: $t = 20$, 100, 200, 300, 400, 500, 600, 700, 800, 900, and 1000°C; $V_{st} = 0$, 0.5, 1, and 1.5%; VR = 30%; w/b = 0.4. Fig. 15 shows the response of SFVSC strength with temperature. At $V_{st} = 1.5\%$, which is the highest volumetric fraction, the temperature increased from 20°C to 800°C, the CS decreased from 44.19 MPa to 23.95 MPa, a decrease of 20.24 MPa; the STS decreased from 3.54 MPa to 1.37 MPa, a decrease of 2.17 MPa. It can be seen from the figure that at different $V_{st}$, the SFVSC strength showed a decreasing trend with temperature increase. The internal damage of concrete intensifies with the increase of temperature causing the strength to decrease all the time with the increase

of temperature treatment.

**Fig.15**

## 5.3 Effect of the steel-fiber volumetric fraction

The effect of $V_{st}$ on strength is studied. The input values were as follows: $t = 20°C$;

$V_{st} = 0, 0.25, 0.5, 0.75, 1, 1.25, 1.5, 1.75$, and 2%; VR = 30, 50, and 70%; and w/b =

0.4. Fig. 16 shows an increasing trend in the SFVSC strength with $V_{st}$. At $V_{st} = 2$%, the

CS and STS of concrete with 30% VR reach 44.29MPa and 3.59MPa, respectively.

However, the rate of increase in the concrete strength curve gradually decreases with

increasing $V_{st}$. For example, the concrete strength increases relatively rapidly for 30%

VR and a $V_{st}$ of 0-1%: the CS and STS increase to 3.84 MPa and 0.49 MPa, respectively.

The concrete strength increases slowly for 1-2% $V_{st}$: the CS and STS increase to 1.83

MPa and 0.09 MPa, respectively. As a result, the 1% volume fraction of steel fibers is

ideal in terms of economic efficiency.

**Fig.16**

## 5.4 Effect of w/b

The effect of w/b on the strength is investigated. The input parameters are $t = 20$,

200, 400, 600, and 800°C; $V_{st} = 1$%; VR = 30%; and w/b = 0.4, 0.45, 0.5, 0.55, and 0.6.

Fig. 17 shows the response of the SFVSC strength with w/b. The higher w/b is, the

lower the concrete strength is, as expected.

**Fig.17**

## 5.5 Sensitivity analysis

Finally, PSO-BPNN is used to conduct a sensitivity test on the residual bearing

capacity of SFVSC subjected to high-temperature treatment to identify the most

important input variables. Table 7 shows the different test datasets created by deleting

one input parameter at a time. The RMSE is a measure of how an input variable affects the output target variable. The results presented in the table show that temperature plays a significant role in predicting the residual bearing capacity of SFVSC subjected to high-temperature treatment.

**Table 7**

## 6. Conclusion

Three models (BPNN, GA-BPNN, and PSO-BPNN) are used in this study to predict the residual bearing capacity of SFVSC. All the data used are obtained from experiments. A comparison of the model predictions with the test values shows satisfactory performance for all computational models for the test stage. The main conclusion drawn from the calculation results is that the PSO-based neural-network model is superior to the other models investigated. Other conclusions are given below.

(1) The prediction model based on the PSO-BP neural network has high accuracy and good adaptability for predicting the mechanical properties of SFVSC subjected to high-temperature treatment. This low-cost and high-efficiency method could be used to further investigate the mechanical properties of lightweight aggregate concrete.

(2) A comparison of the MAPEs and RMSEs of the BPNN, GA-BPNN, and PSO-BPNN predictions shows that the prediction accuracy decreases in the following order: PSO-BPNN > GA-BPNN > BPNN. For example, the MAPE for the PSO-BPNN prediction is less than 2% and below that of the GA-BPNN prediction. The MAPE of the GA-BPNN prediction is less than 6% and below that of the BPNN prediction. The

RMSE of the PSO-BPNN prediction is less than 0.4 and below that of the GA-BPNN prediction. The RMSE between the GA-BPNN prediction and the target value is less than 1.3 and below that of the BPNN prediction.

(3) The BPNN, GA-BPNN, and PSO-BPNN predictions are in good agreement with the target values. The $R^2$ values of the PSO-BPNN CS and STS prediction data of 0.999840 and 0.999513 respectively are closer to 1 than those of the BPNN and GA-BPNN. Thus, PSO-BPNN is more robust than BPNN and GA-BPNN.

(4) A sensitivity analysis shows that the investigated parameters ($t$, VR, w/b, and $V_{st}$) all have large effects on the performance of SFVSC subjected to high-temperature treatment that decrease in the following order: $t >$ VR$>$ w/b$> V_{st}$.

(5) The temperature has the largest influence on the residual bearing capacity of SFVSC subjected to high-temperature treatment. The concrete strength decreases with increasing treatment temperature. For example, when the $V_{st} = 1.5\%$, VR = 30%, w/b = 0.4, increasing the treatment temperature from 20 °C to 800°C, the CS to decrease from 44.19 MPa to 23.95 MPa, corresponding to a decrease of 45.81%.

(6) The CS and STS of SFVSC increase linearly with $V_{st}$ at a fixed VR. This effect is less pronounced for $V_{st}$s above 1%. Thus, $V_{st}$ should not exceed 1% for optimal economic efficiency.

**ACKNOWLEDGEMENTS**

**COMPETING INTERESTS**

**DATA AVAILABILITY**

Some or all data, models, or codes that support the findings of this study are available from the corresponding author upon reasonable request.

**REFERENCES**

[1]. Demirel B, Gultekin E, Alyamac KE. Performance of Structural Lightweight Concrete containing Metakaolin after Elevated Temperature. KSCE Journal of Civil Engineering. 2019;23(7):2997-3004.

[2]. Bingöl AF, Tortum A, Gül R. Neural networks analysis of compressive strength of lightweight concrete after high temperatures. Materials & Design (1980-2015). 2013;52:258-64.

[3]. al-Swaidani AM. Use of micro and nano volcanic scoria in the concrete binder: Study of compressive strength, porosity and sulfate resistance. Case Studies in Construction Materials. 2019;11.

[4]. Contrafatto L. Recycled Etna volcanic ash for cement, mortar and concrete manufacturing. Construction and Building Materials. 2017;151:704-13.

[5]. Djobo JNY, Tchadjié LN, Tchakoute HK, Kenne BBD, Elimbi A, Njopwouo D. Synthesis of geopolymer composites from a mixture of volcanic scoria and metakaolin. Journal of Asian Ceramic Societies. 2018;2(4):387-98.

[6]. Franesqui MA, Yepes J, García-González C. Improvement of moisture damage resistance and permanent deformation performance of asphalt mixtures with marginal porous volcanic aggregates using crumb rubber modified bitumen. Construction and Building Materials. 2019;201:328-39.

[7]. Juimo Tchamdjou WH, Cherradi T, Abidi ML, Pereira-de-Oliveira LA. Mechanical properties of lightweight aggregates concrete made with cameroonian volcanic scoria: Destructive and non-destructive characterization. Journal of Building Engineering. 2018;16:134-45.

[8]. Onoue K, Tamai H, Suseno H. Shock-absorbing capability of lightweight concrete utilizing volcanic pumice aggregate. Construction and Building Materials. 2015;83:261-74.

[9]. Tanyildizi H. Fuzzy logic model for prediction of mechanical properties of lightweight concrete exposed to high temperature. Materials & Design. 2009;30(6):2205-10.

[10]. Getahun MA, Shitote SM, Abiero Gariy ZC. Artificial neural network based modelling approach for strength prediction of concrete incorporating agricultural and construction wastes. Construction and Building Materials. 2018;190:517-25.

[11]. Duan ZH, Kou SC, Poon CS. Prediction of compressive strength of recycled aggregate concrete using artificial neural networks. Construction and Building Materials. 2013;40:1200-6.

[12]. Elshafey AA, Dawood N, Marzouk H, Haddara M. Crack width in concrete using artificial neural networks. Engineering Structures. 2013;52:676-86.

[13]. Liu K, Alam MS, Zhu J, Zheng J, Chi L. Prediction of carbonation depth for recycled aggregate concrete using ANN hybridized with swarm intelligence algorithms. Construction and Building Materials. 2021;301.

[14]. Liu Q, Sun P, Fu X, Zhang J, Yang H, Gao H, et al. Comparative analysis of BP neural network and RBF neural network in seismic performance evaluation of pier columns. Mechanical Systems and Signal Processing. 2020;141.

[15]. Pham BT, Nguyen MD, Dao DV, Prakash I, Ly HB, Le TT, et al. Development of artificial intelligence models for the prediction of Compression Coefficient of soil: An application of Monte Carlo sensitivity analysis. Sci Total Environ. 2019;679:172-84.

[16]. Tenza-Abril AJ, Villacampa Y, Solak AM, Baeza-Brotons F. Prediction and sensitivity analysis of compressive strength in segregated lightweight concrete based on artificial neural network using ultrasonic pulse velocity. Construction and Building Materials. 2018;189:1173-83.

[17]. Xu J, Zhao X, Yu Y, Xie T, Yang G, Xue J. Parametric sensitivity analysis and modelling of mechanical properties of normal- and high-strength recycled aggregate concrete using grey theory, multiple nonlinear regression and artificial neural networks. Construction and Building Materials. 2019;211:479-91.

[18]. Hu H, Tang L, Zhang S, Wang H. Predicting the direction of stock markets using optimized neural networks with Google Trends. Neurocomputing. 2018;285:188-95.

[19]. Ren C, An N, Wang J, Li L, Hu B, Shang D. Optimal parameters selection for BP neural network based on particle swarm optimization: A case study of wind speed forecasting. Knowledge-Based Systems. 2014;56:226-39.

[20]. Zhang Q, Jiang T, Gemmer M, Becker S. Precipitation, temperature and runoff analysis from 1950 to 2002 in the Yangtze basin, China / Analyse des précipitations, températures et débits de 1950 à 2002 dans le bassin du Yangtze, en Chine. Hydrological Sciences Journal. 2005;50(1).

[21]. Awolusi TF, Oke OL, Akinkurolere OO, Sojobi AO, Aluko OG. Performance comparison of neural network training algorithms in the modeling properties of steel fiber reinforced concrete. Heliyon. 2019;5(1):e01115.

[22]. Chandwani V, Agrawal V, Nagar R. Modeling slump of ready mix concrete using genetic algorithms assisted training of Artificial Neural Networks. Expert Systems with Applications. 2015;42(2):885-93.

[23]. Yan F, Lin Z. New strategy for anchorage reliability assessment of GFRP bars to concrete using hybrid artificial neural network with genetic algorithm. Composites

Part B: Engineering. 2016;92:420-33.

[24].    Yan F, Lin Z, Wang X, Azarmi F, Sobolev K. Evaluation and prediction of bond strength of GFRP-bar reinforced concrete using artificial neural network optimized with genetic algorithm. Composite Structures. 2017;161:441-52.

[25].    Ismail A, Jeng DS, Zhang LL. An optimised product-unit neural network with a novel PSO–BP hybrid training algorithm: Applications to load–deformation analysis of axially loaded piles. Engineering Applications of Artificial Intelligence. 2013;26(10):2305-14.

[26].    Qiu R, Wang Y, Wang D, Qiu W, Wu J, Tao Y. Water temperature forecasting based on modified artificial neural network methods: Two cases of the Yangtze River. Sci Total Environ. 2020;737:139729.

[27].    China AbtMoCotPsRo. Technical Specification for Lightweight Aggregate Concrete: Technical Specification for Lightweight Aggregate Concrete; 2002.

[28].    China AbtMoCotPsRo. Standard of Testing Methods for Mechanical Properties of Ordinary Concrete: Standard of Testing Methods for Mechanical Properties of Ordinary Concrete; 2003.

[29].    Montgomery DC, Peck EA, Vining GG. Introduction to linear regression analysis: John Wiley & Sons; 2021.

[30].    al-Swaidani AM, Khwies WT. Applicability of Artificial Neural Networks to Predict Mechanical and Permeability Properties of Volcanic Scoria-Based Concrete. Advances in Civil Engineering. 2018;2018:1-16.

**Table**

**Table 1 Materials used in experiments**

| Material | Information |
|---|---|
| Volcanic scoria | Porous volcanic scoria with a bulk density of 850 kg/m$^3$ that is artificially pulverized to obtain a continuous gradation of 5 to 40 mm. |
| Water | Ordinary tap water. |
| Sand | Common river sand with a bulk density of 1450 kg/m$^3$. |
| Gravel | Common crushed stone with good particle gradation, a size range of 5-40 mm, and a bulk density of 1550 kg/m$^3$. |
| Cement | P.042.5 ordinary silicate cement with a collapse degree of 39 mm, 3- and 28-day strengths of 18 MPa and 46.7 MPa, respectively. |
| Steel fiber | Shear-type steel fiber, 38 mm long, approximately 1 mm wide, and 0.35-0.5 mm thick. |

**Table 2 Chemical composition of volcanic scoria**

| Chemical composition | $SiO_2$ | $AlO_3$ | $TFe_2O_3$ | $CaO$ | $MgO$ | $K_2O$ | $Na_2O$ | $TiO_2$ | $P_2O_5$ | $MnO$ | $LOl$ |
|---|---|---|---|---|---|---|---|---|---|---|---|
| Content (%) | 67.85 | 14.50 | 3.55 | 2.24 | 0.85 | 2.59 | 2.56 | 0.51 | 0.10 | 0.09 | 5.04 |

**Table 3 Mix proportions for volcanic scoria concrete**

| Mix description | Cement (kg/m$^3$) | Sand (kg/m$^3$) | Stone (kg/m$^3$) | Volcanic scoria (kg/m$^3$) | Steel-fiber volumetric fraction/% | w/b |
|---|---|---|---|---|---|---|
| 30%VS | 394.62 | 742.81 | 789.23 | 156.53 | [0-1.5] | 0.4 |
| 50%VS | 394.62 | 742.81 | 563.74 | 260.88 | [0-1.5] | 0.4 |
| 70%VS | 394.62 | 742.81 | 338.24 | 365.23 | [0-1.5] | 0.4 |
| 30%VS | 394.62 | 726.84 | 772.79 | 155.83 | [0-1.5] | 0.5 |
| 50%VS | 394.62 | 726.84 | 551.99 | 259.71 | [0-1.5] | 0.5 |
| 70%VS | 394.62 | 726.84 | 331.20 | 363.60 | [0-1.5] | 0.5 |

W/b = Water-to-cement ratio

**Table 4 The relationship between the number of hidden nodes and RMSE of the GA-BPNN and PSO-BPNN simulation results**

| Hidden nodes | 4 | 5 | 6 | 7 | 8 | 9 | 10 | 11 | 12 | 13 |
|---|---|---|---|---|---|---|---|---|---|---|
| BPNN1 | 3.0225 | 2.8337 | 2.8274 | 2.6934 | 2.9029 | 2.9914 | 3.0150 | 3.0614 | 3.0951 | 3.1732 |
| BPNN2 | 0.2795 | 0.2783 | 0.2675 | 0.2676 | 0.2736 | 0.2894 | 0.2983 | 0.2984 | 0.3004 | 0.3079 |

**Table 5 Comparison of the predictive performance of BPNN, GA-BPNN, and PSO-BPNN**

| Prediction Model | Maximum absolute | Minimum absolute | Maximum relative error/% | Minimum relative | MAPE/% | RMSE |
|---|---|---|---|---|---|---|

| | error | error | | error/% | | |
|---|---|---|---|---|---|---|
| BPNN1 | 4.4565 | -3.3573 | 11.86 | 2.56 | 7.33 | 1.9703 |
| BPNN2 | 0.3599 | -0.3384 | 11.58 | 1.53 | 7.56 | 0.1763 |
| GA-BPNN1 | 2.8644 | -1.4733 | 9.98 | 0.43 | 4.43 | 1.2868 |
| GA-BPNN2 | 0.2337 | -0.1477 | 8.34 | 0.87 | 5.10 | 0.1137 |
| PSO-BPNN1 | 0.9556 | -0.8791 | 3.97 | 0.05 | 1.01 | 0.3332 |
| PSO-BPNN2 | 0.1551 | -0.1081 | 4.25 | 0.02 | 1.62 | 0.0488 |

**Table 6 Robustness of BPNN, GA-BPNN, and PSO-BPNN**

| Models | Training data $R^2$ | Test data $R^2$ |
|---|---|---|
| BPNN1 | 0.990106 | 0.994141 |
| BPNN2 | 0.986012 | 0.993345 |
| GA-BPNN1 | 0.990790 | 0.997506 |
| GA-BPNN2 | 0.989881 | 0.997256 |
| PSO-BPNN1 | 0.992556 | 0.999840 |
| PSO-BPNN2 | 0.997038 | 0.999513 |

**Table 7 Sensitivity analysis using the PSO-BPNN model for the testing stage.**

| Target strength | Input combination | | | | Target | Statistical indices |
|---|---|---|---|---|---|---|
| | VR(%) | t(°C) | $V_{st}$(%) | w/b | | RMSE |
| **Compressive strength** | - | + | + | + | + | 2.6033 |
| | + | - | + | + | + | **4.7370** |
| | + | + | - | + | + | 1.0164 |
| | + | + | + | - | + | 1.4874 |
| **Split tensile strength** | - | + | + | + | + | 0.2296 |
| | + | - | + | + | + | **0.6198** |
| | + | + | - | + | + | 0.0741 |
| | + | + | + | - | + | 0.1664 |

A. "+" and "-" indicate variables used and removed from the model, respectively.
B. Bolded values indicate the statistical information of the most significant variables.
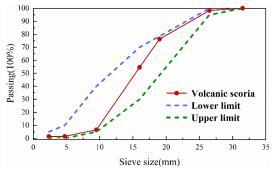
**Figures**



**Fig.1.** Materials

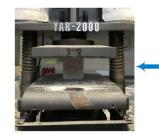**Fig.2.** Particle-size distribution and physical properties of the aggregates



(a) The preparation process of SFVSC



(b) Test flow diagram
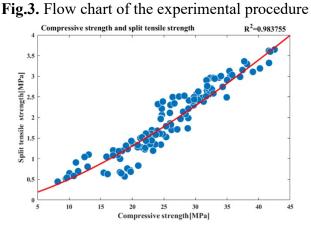
**Fig.3.** Flow chart of the experimental procedure



**Fig.4.** Correlation between the split tensile strength and compressive strength of SFVSC
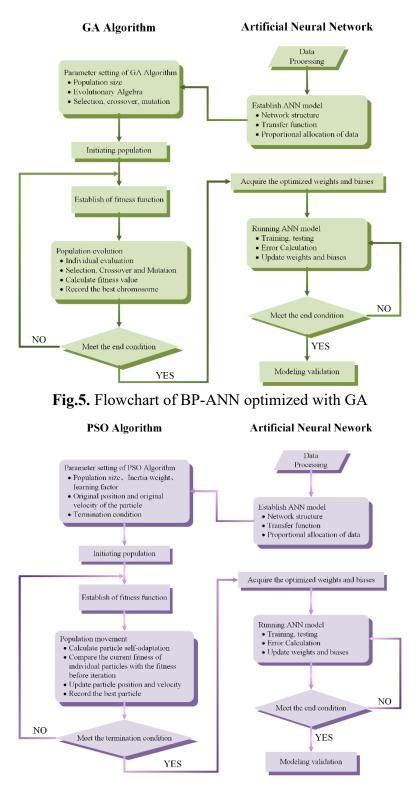
**Fig.5.** Flowchart of BP-ANN optimized with GA
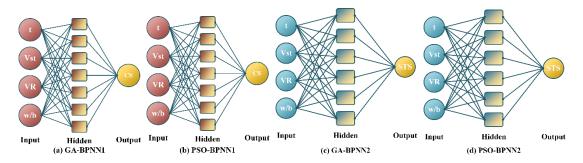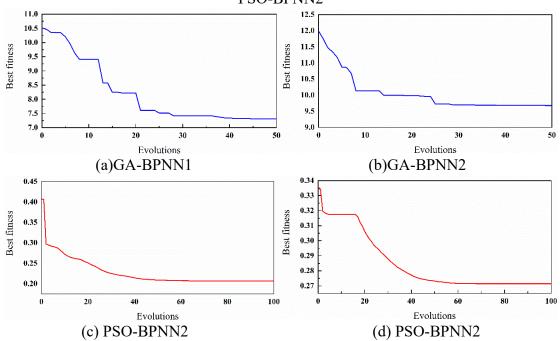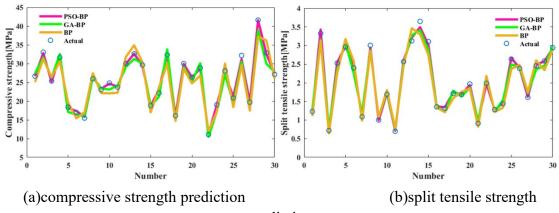


**Fig.6.** Flowchart of BP-ANN optimized with PSO

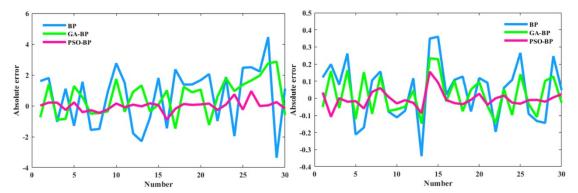**Fig.7.** Architecture of ANN: (a) GA-BPNN1; (b) PSO-BPNN1; (c) GA-BPNN2; (d) PSO-BPNN2



(a)GA-BPNN1      (b)GA-BPNN2

(c) PSO-BPNN2      (d) PSO-BPNN2

**Fig.8.** Average fitness curve with evolutionary generations: (a) GA-BPNN1; (b) GA-BPNN2; (c) PSO-BPNN1; (d) PSO-BPNN2



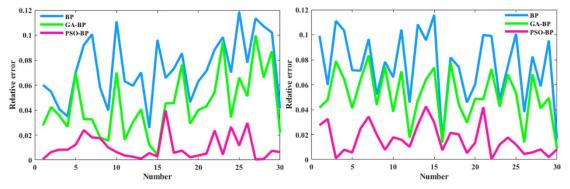(a)compressive strength prediction      (b)split tensile strength prediction
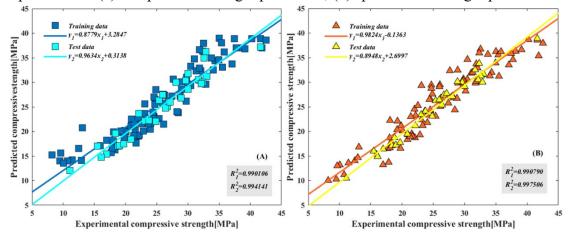
**Fig.9.** Comparison of BPNN, GA-BPNN, and PSO-BPNN predictions: (a) compressive strength prediction; (b) split tensile strength prediction

(a) compressive strength prediction       (b) split tensile strength prediction

**Fig.10.** Comparison of errors in BPNN, GA-BPNN, and PSO-BPNN predictions: (a) compressive strength prediction; (b) split tensile strength prediction



(a) compressive strength prediction       (b) split tensile strength prediction

**Fig.11.** Comparison of relative errors in BPNN, GA-BPNN, and PSO-BPNN predictions: (a) compressive strength prediction; (b) split tensile strength prediction
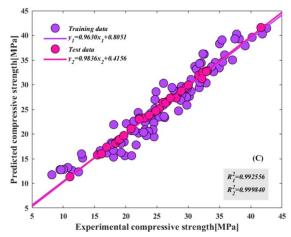
**Fig.12.** Comparison of actual compressive strength and ANN prediction: (A) BPNN; (B) GA-BPNN; (C) PSO-BPNN
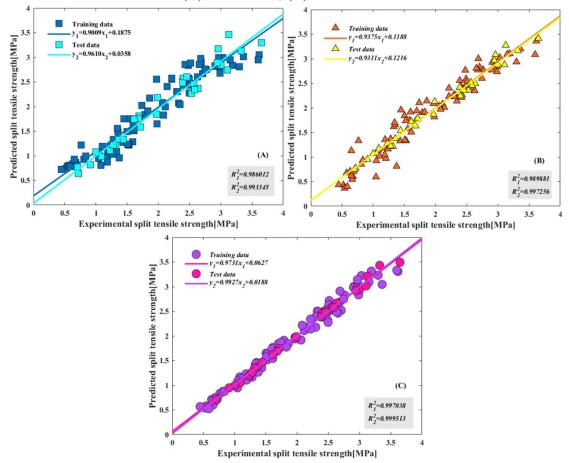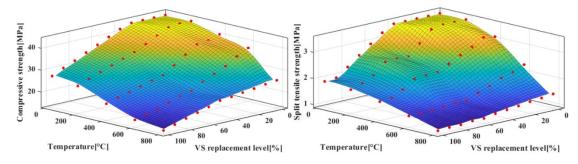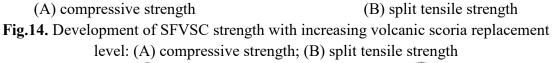


**Fig.13.** Comparison of actual split tensile strength and ANN prediction: (A) BPNN2; (B)GA-BPNN2; (C) PSO-BPNN2

(A) compressive strength　　　　　　　　(B) split tensile strength

**Fig.14.** Development of SFVSC strength with increasing volcanic scoria replacement level: (A) compressive strength; (B) split tensile strength



(A) compressive strength　　　　　　　　(B) split tensile strength

**Fig.15.** Development of SFVSC strength with increasing temperature: (A) compressive strength; (B) split tensile strength



(A) compressive strength　　　　　　　　(B) split tensile strength

**Fig.16.** Development of SFVSC strength with increasing steel-fiber volumetric fraction: (A) compressive strength; (B) split tensile strength



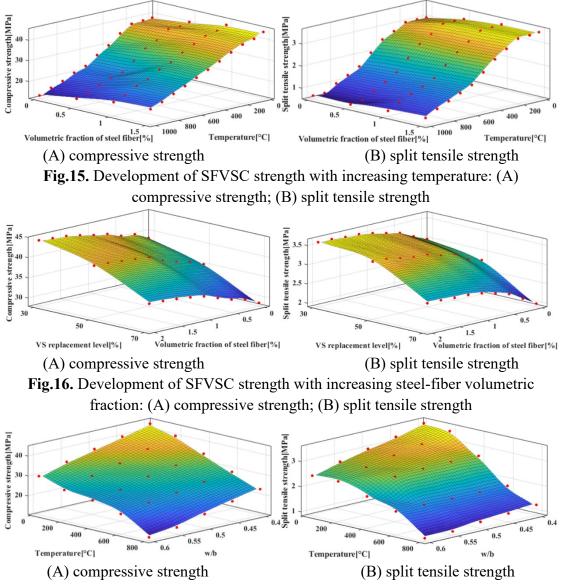(A) compressive strength　　　　　　　　(B) split tensile strength

**Fig.17.** Development of SFVSC strength with increasing w/b: (A) compressive strength